

# Millimeter wave scattering from ice crystals and their aggregates: Comparing cloud model simulations with X- and Ka-band radar measurements

Giovanni Botta,<sup>1,2</sup> Kultegin Aydin,<sup>2</sup> Johannes Verlinde,<sup>1</sup> Alexander E. Avramov,<sup>3</sup> Andrew S. Ackerman,<sup>4</sup> Ann M. Fridlind,<sup>4</sup> Greg M. McFarquhar,<sup>5</sup> and Mengistu Wolde<sup>6</sup>

Received 4 March 2011; revised 10 June 2011; accepted 14 June 2011; published 15 September 2011.

[1] Arctic clouds are often mixed-phase, such that the radiative properties of the clouds are a strong function of the relative amounts of cloud liquid and ice. Modeling studies have shown that the poorly understood ice phase processes are the regulators of the liquid water fraction. However, evaluating the fidelity of the model ice parameterizations has proven to be a difficult task. This study evaluates results of different ice microphysics representations in a cloud resolving model (CRM) using cloud radar measurements. An algorithm is presented to generate realistic ice crystals and their aggregates from which radar backscattering cross sections may be calculated using a generalized solution for a cluster of spheres. The aggregate is composed of a collection of ice crystals, each of which is constructed from a cluster of tiny ice spheres. Each aggregate satisfies the constraints set by the component crystal type and the mass-dimensional relationship used in the cloud resolving model, but is free to adjust its aspect ratio. This model for calculating radar backscattering is compared to two spherical and two spheroidal (bulk model) representations for ice hydrometeors. It was found that a refined model for representing the ice hydrometeors, both pristine crystals and their aggregates, is required in order to obtain good comparisons between the CRM calculations and the radar measurements. The addition of the radar-CRM comparisons to CRM-in situ measurements comparisons allowed conclusions about the appropriateness of different CRM ice microphysics parameterizations.

**Citation:** Botta, G., K. Aydin, J. Verlinde, A. E. Avramov, A. S. Ackerman, A. M. Fridlind, G. M. McFarquhar, and M. Wolde (2011), Millimeter wave scattering from ice crystals and their aggregates: Comparing cloud model simulations with X- and Ka-band radar measurements, *J. Geophys. Res.*, 116, D00T04, doi:10.1029/2011JD015909.

## 1. Introduction

[2] The recent assessments by the Intergovernmental Panel on Climate Change [Intergovernmental Panel on Climate Change (IPCC), 2007] report indicated that cloud-aerosol interactions on climate and the cloud response to climate forcing represent the greatest uncertainties in predicting climate changes. These cloud-aerosol processes operate on scales much smaller than even the highest resolution

General Circulation Models (GCMs), requiring use of high resolution Cloud Resolving Models (CRMs) using sophisticated parameterizations of cloud physical processes to address questions about specific cloud processes. Unfortunately, these models markedly disagree among themselves and observations in studies of arctic cloud processes (see inter-comparison papers by Klein *et al.* [2009] and Morrison *et al.* [2009]), leading to further debates about which are the dominant physical processes controlling the characteristics of these clouds [Fridlind *et al.*, 2007; Avramov and Harrington, 2010; de Boer *et al.*, 2010]. Well-constructed observational data sets are needed to drive and evaluate results from these CRM simulations in order to improve parameterizations of the physical processes. Radar is one of the few observing systems that provides continuous observations of large spatial extent of cloud systems, with the additional advantage that the sampling resolution is similar to CRM grid-volumes, but comparisons require a transformation from model variable space (e.g., distribution parameters of complex hydrometeors) to radar measurement space (e.g., radar reflectivity).

<sup>1</sup>Department of Meteorology, Pennsylvania State University, University Park, Pennsylvania, USA.

<sup>2</sup>Department of Electrical Engineering, Pennsylvania State University, University Park, Pennsylvania, USA.

<sup>3</sup>Department of Earth, Atmospheric, and Planetary Sciences, Massachusetts Institute of Technology, Cambridge, Massachusetts, USA.

<sup>4</sup>NASA Goddard Institute for Space Studies, New York, New York, USA.

<sup>5</sup>Department of Atmospheric Sciences, University of Illinois at Urbana-Champaign, Urbana, Illinois, USA.

<sup>6</sup>Flight Research Laboratory, Institute for Aerospace Research, National Research Council, Ottawa, Ontario, Canada.

[3] Interpretation of radar measurements of clouds and precipitation requires an accurate understanding of the electromagnetic scattering characteristics of hydrometeors. Several different computation techniques are available for scattering from pristine ice crystals such as the discrete dipole approximation (DDA), the finite difference time domain (FDTD), and the generalized multiparticle Mie (GMM) methods [O'Brien and Goedecke, 1988; Xu, 1995; Tang and Aydin, 1995; Aydin and Walsh, 1999; Mishchenko et al., 2002; Liu, 2008; Grecu and Olson, 2008; Botta et al., 2010]. Aydin and Walsh [1999] provided parameters for fitted curves for backscattering cross sections (computed using the FDTD method) of hexagonal columns, hexagonal plates, stellar crystals, and 4-, 6-, and 8-branch bullet rosettes at 35, 94, and 220 GHz frequencies. Liu [2008] generated an extensive scattering database using the DDA method for 11 crystal shapes, including dendrites, over the frequency range 15 to 350 GHz.

[4] Until recently highly complex shaped hydrometeors, such as ice crystal aggregates, have been modeled using an equivalent representation of their dielectric properties through, e.g., the Maxwell Garnet formula [Bohren and Battan, 1980]. This "bulk model" (or "soft sphere" model) approach consists of modeling an aggregate as a sphere or spheroid composed of a mixture of ice and air (and water in the case of mixed-phase hydrometeors like melting hailstones or snowflakes). This approach has been used at microwave frequencies for simulating the radar scattering properties of ice phase hydrometeors and has worked well for dense particles such as hail and graupel at the lower microwave frequencies [Marshall and Gunn, 1952; Battan and Herman, 1962; Bohren and Battan, 1980; Aydin et al., 1984; Aydin and Seliga, 1984; Longtin et al., 1987; Meneghini and Liao, 1996]. Matrosov [2007] has modeled snowflakes with the same approach for frequencies up to 94 GHz. The Mie or T-Matrix techniques are generally used for scattering computations from spherical and spheroidal shaped particles [Mishchenko et al., 2002]. One of the main limitations of this approach in representing a heterogeneous particle (e.g., a snowflake) as a homogeneous one is resonance effects. These resonance effects result in oscillations in the backscattering cross sections for particles comparable in dimension to half a wavelength and larger. A homogeneous particle with a smooth shape such as a sphere or spheroid enhances these resonance effects. However, the complex irregular structure of ice crystal aggregates is not well represented by homogeneous spheres or spheroids as shown by Botta et al. [2010] and Petty and Huang [2010].

[5] There are very few papers in the literature dealing with microwave scattering from complex aggregate models. None of these exhibits the strong resonance effects observed for spheres and spheroids. For example, Osharin [1994] computed extinction and absorption cross sections of one aggregate (composed of five dendrite-like crystals) of radius 1.78 mm over the frequency range 10 to 130 GHz using the DDA technique. An equivalent sphere model was found to match the extinction cross sections reasonably well, but not the absorption cross sections.

[6] Ishimoto [2008] modeled aggregates using a fractal approach and performed backscattering cross section computations with the FDTD method at 9.8, 35, and 95 GHz for ice particles with diameters up to 20 mm. It was

observed that the backscattering cross sections of the fractal aggregates were lower than those of the equal volume sphere models.

[7] Westbrook et al. [2006], modeled aggregates of bullet rosettes with maximum dimensions less than 3.5 mm. Radar cross section computations were performed at 35 and 94 GHz frequencies using the Rayleigh-Gans theory by splitting the aggregate into small volume elements and treating each element as a Rayleigh scatterer and ignoring interactions between these elements. It was concluded that an ice-air sphere with matched radius of gyration produces acceptable scattering results for aggregates with maximum dimension up to 1.7 mm, which is just above half the wavelength at 94 GHz ( $\lambda = 3.19$  mm).

[8] Petty and Huang [2010] considered four aggregates, one composed of needles and the other three of dendritic crystals. By changing a scaling parameter it was possible to generate a range of size and mass values for these four shapes. A modified version of DDA for sparse structures was used for scattering computations. It was concluded that: "...even when spheres of nonequal mass are considered, there is no single combination of density and particle mass that simultaneously captures the multifrequency properties of these aggregates on a per-mass basis. We therefore find no persuasive basis for retaining any kind of soft sphere, equal mass or otherwise, as a model for the microwave properties of snowflakes."

[9] Botta et al. [2010] generated aggregates of columnar crystals to study their scattering characteristics (at 3 and 35 GHz) above and through the melting layer using the generalized multiparticle Mie (GMM) method [Xu, 1995]. Ten random realizations of aggregates were averaged for each size, which ranged between 2.5 to 10 mm for dry aggregates. At 35 GHz the oblate spheroidal model produced radar cross sections that were more than 7 dB lower for sizes greater than 3 mm (which is just below half the wavelength at 35 GHz) and exhibited the oscillatory behavior as a function of size, which is characteristic of resonance scattering. This was not observed with the columnar crystal aggregates.

[10] This study deals with observations from arctic mixed-phase clouds, where the dominant contribution to radar reflectivity is due to ice hydrometeors. In the particular case considered here the ice particles are dendritic crystals and their aggregates, with sizes exceeding half the wavelength at 35 GHz and reaching half the wavelength at 9 GHz. Given these circumstances, a direct comparison of CRM-derived and measured radar reflectivities requires due consideration of the electromagnetic scattering calculations of the ice hydrometeors. A single layer, mixed-phase cloud observed on April 8th, 2008 during the Indirect and Semi-Direct Aerosol Campaign (ISDAC) [McFarquhar et al., 2011] is the subject of this study. The CRM study of this case is described in detail by Avramov et al. [2011]; this paper presents the electromagnetic scattering calculations.

## 2. Description of Radar Measurements and Cloud Model

[11] ISDAC was conducted in the vicinity of the DOE-ARM Climate Research Facility (ACRF) site at Barrow, AK in April 2008. Observing systems pertinent to this study

include the Barrow ACRF vertically pointing 35 GHz (Ka-band) millimeter cloud radar (MMCR) [Moran *et al.*, 1998] and the National Research Council (NRC) of Canada Convair-580 equipped with the NRC Airborne W-band (94 GHz) and X-band (9.41 GHz) Radar (NAWX) [Wolde and Pazmany, 2005] and an unprecedented 41 cloud microphysics and aerosol instruments. Barrow MMCR data from two half-hour periods on April 8th, 2008 (17:00 – 17:30 UTC and 22:30 – 23:00 UTC) and the NRC-Convair X-band data from a flight on the same day (Flight 16) are the subjects of analysis. On this day a single-layer, mixed-phase cloud was observed along the North Slope midway between the ridge-line of a northwestward moving high pressure system over the Arctic Ocean and a weakening low to its west. The clouds existed along the southern and western edge of the upper level ridge, covering most of the North Slope of Alaska and extending well to the north and west of Barrow over the Arctic Ocean. The case is discussed in detail by McFarquhar *et al.* [2011] and Avramov *et al.* [2011]. This paper evaluates results from the CRM modeling study described by Avramov *et al.* [2011] using the two radar systems.

[12] Data from the MMCR boundary layer mode [Kollias *et al.*, 2007] only were used; reflectivities were adjusted by 9.8 dBZ for the known offset in calibration of the radar [Protat *et al.*, 2011]. Only X-band radar data from the dual-frequency Convair radars were used: the W-band radar was not functioning during this flight. Profiles of X-band data were collected while the aircraft was executing a series of porpoising maneuvers consisting of ramped ascents and descents through the cloud layer between 22:27–23:00 UTC along a 100 km transect from Barrow toward the northwest over the ocean. The X-band data were cleaned using the NRC cloud mask scheme. All pixels identified as noise, ground and ground contaminated pixels were eliminated from the analysis. The reflectivity errors for both radars are estimated to be less than 2 dB. Of the Convair in situ measurements, the PMS 2D-P and SPEC 2D-S optical array probes were used to infer ice particle size distributions for 10 s segments of flight. To minimize problems associated with ice shattering on probe inlets only ice particles with maximum dimension greater than 100  $\mu\text{m}$  were considered. Images from the Cloud Particle Imager (CPI) were used to assist in ice particle habit identification.

[13] The Cloud Resolving Model (CRM) used in this study is the Distributed Hydrodynamic Aerosol-Radiation-Microphysics Application (DHARMA). DHARMA consists of a large-eddy simulation (LES) dynamical core [Stevens *et al.*, 2002] with size-resolved bin microphysics [Ackerman *et al.*, 1995; Fridlind *et al.*, 2007] and a two-stream, 44 wavelength radiative transfer model [Toon *et al.*, 1989]. The latest addition to the model, which makes it very suitable for mixed-phase cloud simulations, is an integrated treatment of cloud particle fall speeds and gravitational collection rates [Böhm 1989, 1992a, 1992b, 1992c, 1994, 1999, 2004]. The simulations analyzed here are described in more detail by Avramov *et al.* [2011, section 5].

[14] The transfer function from model output to radar measurements requires careful consideration. The CRM microphysical prognostic variables are number concentration per unit mass of hydrometeors in mass-doubling intervals (bins). The various microphysical processes

transfer mass between bins at a specified grid-volume, while advection and sedimentation of hydrometeors move mass from grid-volume to grid-volume. The hydrometeor sedimentation velocity depends on the particle's mass, maximum dimension, cross-sectional area, and aspect ratio [Böhm, 1992a, 1999]. The characteristic cross-sectional area for each mass bin is diagnosed from a specified area-dimensional relationship, where the (maximum) dimension is determined from a mass-dimensional relationship. The radar backscatter is a strong function of the mass and the maximum dimension of the aggregate. The hydrometeors constructed to calculate the radar backscattering cross section must therefore satisfy both the mass and mass-dimensional relationship employed in the CRM to be consistent with the model physics. The model microphysical processes may then be evaluated by comparing the model-produced hydrometeor size distributions to both in situ and radar measurements of the cloud system being modeled. The model produced separate distributions for pristine ice crystals and aggregates of ice crystals; however, in situ ice measurements do not distinguish between the two classes. For comparison with the radar measurements it is necessary to characterize the scattering properties of both hydrometeor classes.

[15] The microphysical representations of the ice crystals and ice crystal aggregates are based on assessment of the in situ measurements. Individual ice crystals are predominantly of dendritic type, while the aggregates are the result of aggregation of simple crystals with no riming effects. Avramov *et al.* [2011] explored the sensitivity of CRM simulations of the April 8th ISDAC case to different mass-dimensional relationships to describe both pristine ice and aggregates. The two different mass-dimensional relationships used to describe the aggregates are those for aggregates of ordinary dendritic crystals (P1e, denoted as low density) [Kajikawa, 1989], and “aggregates of thin plates” (denoted as high density) [Mitchell and Heymsfield, 2005; Mitchell *et al.*, 1990]. The two different mass-dimensional relationships for pristine ice are those for stellar crystals (P1d, denoted as low density) and broad branched crystals (P1c, denoted as high density) by Mitchell [1996]. Figure 1 shows these four mass-dimensional relationships: Figure 1 (left) shows the two mass-dimensional relationships for aggregates (solid lines), while Figure 1 (right) shows the two pristine crystal mass-dimensional relationships. Different choices of mass-dimensional relationship for pristine ice crystals and aggregates not only impact the CRM simulations, but also the modeling of electromagnetic scattering by ice hydrometeors.

### 3. Pristine Crystal and Aggregate Modeling Using the Generalized Multiparticle Mie (GMM) Method

[16] The ice crystal and ice crystal aggregate modeling technique presented in this work employs the Generalized Multiparticle Mie (GMM) method [Xu, 1995]. GMM is an analytical solution of Maxwell's equations for a cluster of arbitrarily located, non-overlapping spheres, each with arbitrary size and dielectric constant. This method has been shown to be in very good agreement with experimental measurements [Xu and Gustafson, 2001] and has been used by Grecu and Olson [2008] and Botta *et al.* [2010] for

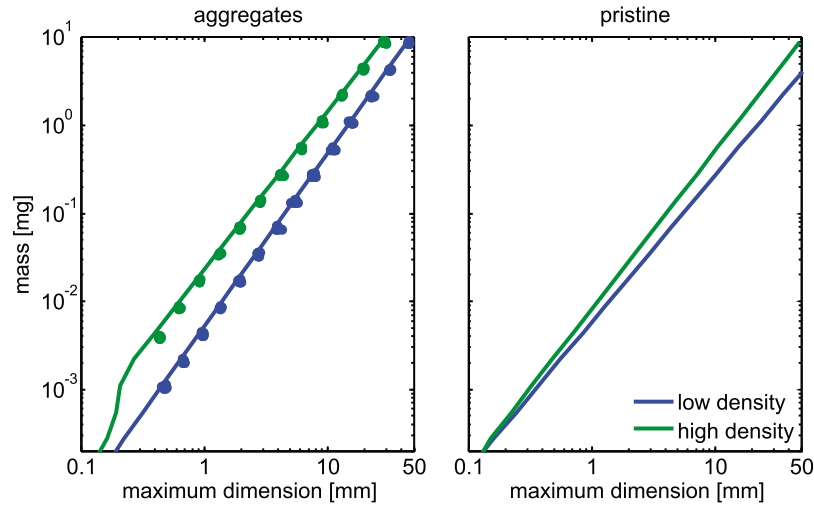


**Figure 1.** Mass-dimensional relationships for (left) low density aggregates (aggregates of P1e crystals [Kajikawa, 1989]) and high density aggregates (“aggregates of thin plates” [Mitchell and Heymsfield, 2005; Mitchell *et al.*, 1990]), and (right) low density pristine crystals (P1d) and high density pristine crystals (P1c), [Mitchell, 1996]. In Figure 1 (left) the solid lines are theoretical mass-dimensional relationships, while each cluster of dots represents 10 random aggregate realizations for the corresponding mass bin; and for both relationships, aggregate mass and maximum dimension are within 5% and 3% of the prescribed values, respectively.

scattering from dry and melting ice crystals and ice crystal aggregates.

### 3.1. Pristine Crystals

[17] Pristine crystals such as hexagonal columns, hexagonal plates and stellar crystals can be modeled from a three dimensional cluster of tiny ice spheres that conform to the crystal shape and dimensions. This is a realistic representation which is comparable in its degree of detail to the models based on the DDA technique [e.g., Liu, 2008]. A comparison of the backscattering cross sections (at vertical incidence) of stellar crystals calculated using the GMM method and the FDTD method [Aydin and Walsh, 1999] showed good agreement, i.e., within 0.5 to 2 dB at 35 GHz and 0.75 to 2.2 dB at 94 GHz for sizes up to 2 mm. In this comparison the GMM method was applied to stellar crystals (P1d, central plate maximum dimension 0.3 mm) with the same mass-dimensional relationship used by Aydin and Walsh [1999] and produced lower backscattering cross section values.

[18] The critical microphysical parameters that determine the radar scattering characteristics of ice particles are their mass, size, and shape. The approach described above can generate any specified mass-dimensional relationship for a given crystal type and was used to generate two sets of pristine ice crystals conforming to the mass-dimensional relationships used in the CRM model (Figure 1, right). For comparison purposes, a second model was used to calculate the scattering from pristine ice crystals. This model is the often used Mie formulation for a sphere with diameter equal to the maximum dimension of the crystal and dielectric properties calculated using the Maxwell Garnet formula with air being the host and ice the inclusion and the volume fraction the ratio of the ice volume to the sphere volume, i.e., a “bulk model” approximation, which is similar to the

one used by Haynes *et al.* [2007]. This representation accurately captures size and mass of the crystals, but not their shapes. Figure 2 shows a representation of a small stellar crystal and the corresponding spherical bulk model. A third possible approach to obtaining the backscattering cross sections of pristine crystals would be to use those available in the literature, such as by Aydin and Walsh [1999] and Liu [2008]. In this case the shape is well represented, but one must choose between matching size or mass.

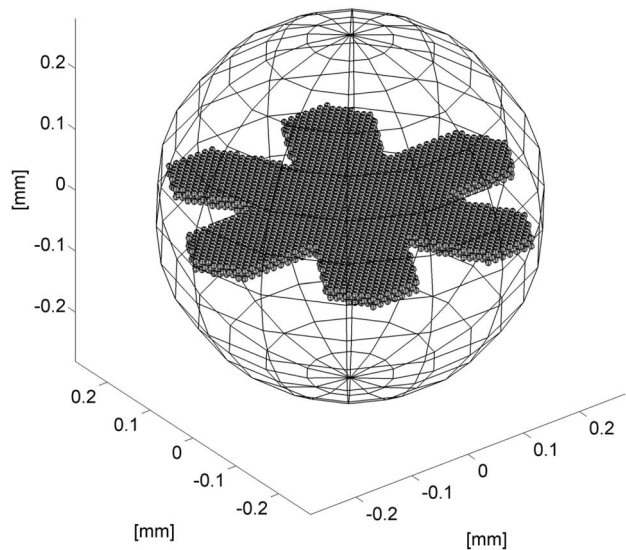


**Figure 2.** A small pristine stellar crystal model composed of almost 6000 tiny ice spheres used in the GMM computations and the circumscribing sphere (in wireframe) used for bulk model computations.

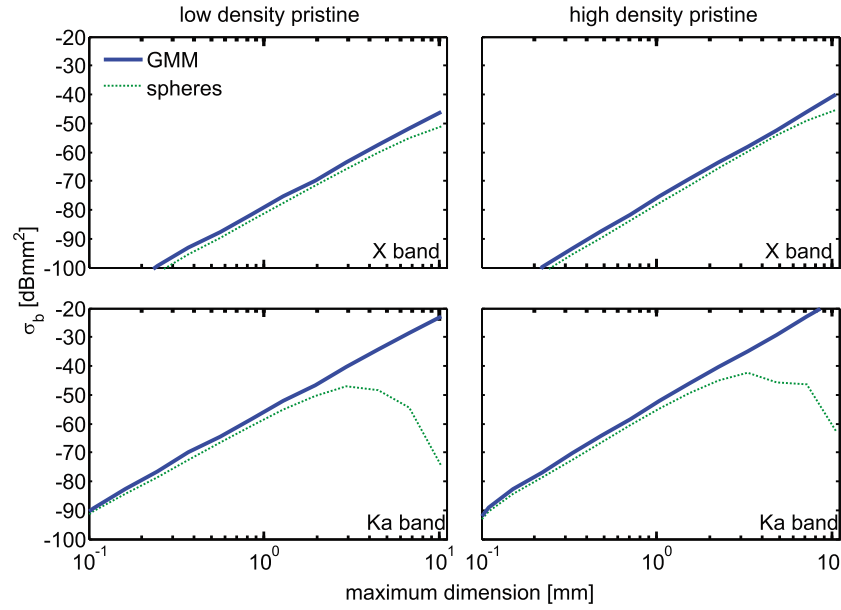


**Figure 3.** Backscattering cross sections ( $\sigma_b$ ) of pristine crystals at vertical incidence computed using the GMM method (stellar crystals) and a spherical bulk model. The low density and high density models correspond to mass-dimensional relationships for P1d and P1c crystals given by *Mitchell* [1996] (Figure 1, right).

[19] Figure 3 shows the backscattering cross sections ( $\sigma_b$ ) for the pristine ice models used in this work. The observed P1c and P1d crystals are both modeled using stellar crystals with central plate maximum dimension 0.3 mm (Figure 2). Sensitivity tests show negligible impact ( $<0.5$  dB) on the scattering cross section at X- and Ka-band for central plate maximum dimension ranging between 0.2 mm and 0.8 mm. Note the increase in  $\sigma_b$  resulting from the use of a high density mass-dimensional relationship. The spherical model representation of pristine crystals underestimates their backscattering cross sections as compared with the more realistic model using the GMM method for both low and high density crystals. In contrast to these,  $\sigma_b$  results taken from a published library [*Liu*, 2008] (<http://cirrus.met.fsu.edu/research/scatdb.html>, “dendrite snowflakes”) by matching sizes are much higher because of the larger mass at each crystal size that results from the particular mass-dimensional relationship used in those calculations. Matching size was selected over matching mass because size is an observed quantity.

### 3.2. Ice Crystal Aggregates

#### 3.2.1. Aggregate Modeling Using Clusters of Spheres

[20] An aggregate is represented by a collection of pristine ice crystals each of which is modeled as a cluster of tiny ice spheres [*Botta et al.*, 2010]. The constituent pristine crystals have random orientation, position and size. However, the cluster of spheres forming the aggregate must satisfy constraints on its maximum dimension and mass within specified tolerances. The basic assumption of this approach is that the scattering properties of an aggregate can be approximated by this cluster of spheres representing the original aggregate. This is a reasonable approximation as long as the spheres in the cluster are distributed in a manner that closely resembles the mass distribution of the original aggregate and

are small enough to reproduce the microphysical properties of the constituent ice crystals (i.e., crystal length/width relationship). The diameters of the spheres in the aggregates considered in this paper do not exceed  $\lambda/40$  at Ka-band ( $\lambda = 8.4$  mm).

[21] The aggregates modeled in this paper are constructed using stellar crystals of type P1d [*Pruppacher and Klett*, 1997, p. 45]. Each crystal is composed of three identical linear arrays of solid ice spheres sharing a common central sphere (Figure 4a). The stellar crystals used in this study are characterized by the width-length ( $w$ - $L$ ) relationship, where  $w$  is the thickness of the stellar crystal and  $L$  is its maximum dimension, given by *Pruppacher and Klett* [1997, p. 51]:

$$w = 0.038L^{0.415}.$$

Each sphere in the stellar crystal with length  $L$  has a diameter equal to  $w$ , and each branch of the stellar crystal is formed from a linear array of such spheres as shown in Figure 4a. This simplified model of a stellar crystal contains its essential shape and mass properties and makes it possible to generate the mass-dimensional relationships used in the CRM simulations.

[22] The mass of the aggregate is the total ice mass of the spheres in the cluster. The size and shape are defined by means of two parameters: maximum dimension, which is the maximum horizontal dimension of the cluster, and aspect ratio, which is the ratio of the maximum vertical to the maximum horizontal dimensions. ‘Horizontal’ and ‘vertical’ directions are defined with respect to the ground, and the aggregates are assumed to fall with their maximum dimension aligned horizontally, i.e., parallel to the ground. For each set of parameters (mass, maximum dimension and aspect ratio) a set of random aggregate realizations is generated [*Botta et al.*, 2010].



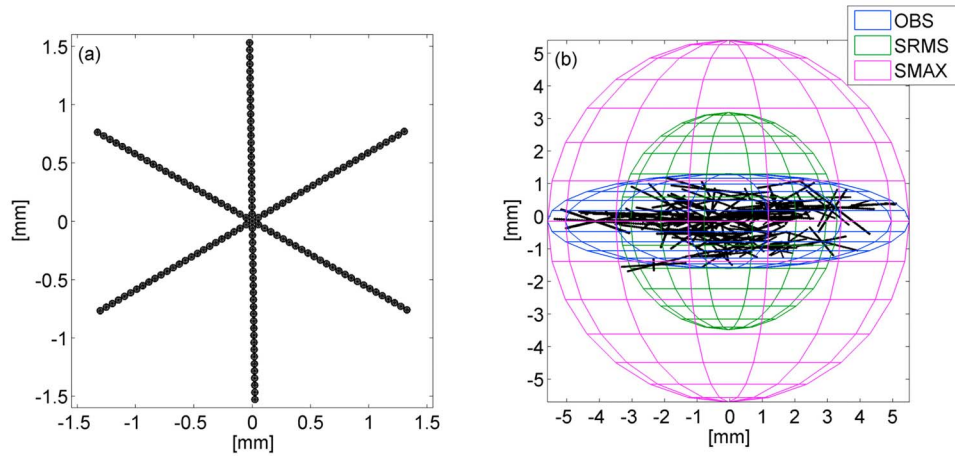


**Figure 4.** (a) Example of a constituent ice crystal composed of 151 spheres each with diameter 0.031 mm and (b) example of an aggregate realization with superimposed bulk model spheres and spheroid (in wireframe). The three bulk models in are: an oblate spheroid model (OBS), a circumscribing sphere (SMAX), both with maximum dimension equal to the maximum dimension of the aggregate, and a sphere with an equivalent radius based on the root-mean square distance of the particle mass from the center of gravity of the aggregate (SRMS). Not shown in the plot is the bulk model OBS06, which is an oblate spheroid similar to OBS but with a fixed aspect ratio of 0.6.

[23] The aggregate generation algorithm creates each realization by adding one crystal at a time. Each new crystal is taken from a distribution of random lengths ( $L$ ) and has a random orientation determined by the three Euler angles (the convention ZZZ was used [e.g., Goldstein *et al.*, 2001, section 4.4]). A randomly selected sphere in the aggregate determines the location of the center of the new crystal. This is to ensure that the cluster is always connected. When spheres overlap in the structure, the smallest sphere is removed. In order to constrain the size of the aggregate, spheres lying outside of a reference spheroid centered in the center of mass of the aggregate are removed. This reference spheroid is based on the desired maximum dimension and aspect ratio of the aggregate and provides an upper bound for both. In fact, the algorithm allows the aspect ratio to adjust below the specified value to meet the combined constraints set by the component crystal type and the mass-dimensional relationship for the aggregate. This process is continued until the mass of the aggregate is within the specified tolerance. Figure 5 shows the aspect ratio for both low and high density aggregates generated by this method.

[24] The distribution of crystal length  $L$  used to generate low density aggregates is Gaussian with an average given by  $L_{avg} = 0.5D_{max}$  for  $D_{max} < 30$  mm and  $L_{avg} = D_{max} - 15$  mm for  $D_{max} \geq 30$  mm and a standard deviation given by  $L_{std} = 0.375D_{max}$ , where  $D_{max}$  is the maximum dimension of the aggregate. The crystal canting is given by a Gaussian distribution with zero average and standard deviation of  $10^\circ$ . For high density aggregates, the Gaussian distribution has an average  $L_{avg} = 0.5D_{max}$  for  $D_{max} < 8$  mm and  $L_{avg} = 4$  mm for bigger sizes, while the canting has a standard deviation of  $25^\circ$ .

[25] For the low density case it turns out to be impossible for the algorithm to generate very large aggregates with a very small amount of mass without increasing the average size of the constituent crystals, which may become unreal-

istically big for aggregates larger than 10 mm. This also leads to very flat aggregate shapes, as shown in Figure 5 (blue dots). This is considered to be a reasonable approximation representing the mass distribution in the aggregate while maintaining the general shape of the constituent crystals. Examples of low and high density aggregate realizations with the same mass are shown in Figure 6.

[26] For each mass-dimensional relationship a set of size/mass bins is selected (14 for the low density case, between 0.45 and 44 mm maximum dimension; 12 for the high density case, between 0.4 and 30 mm maximum dimension) and for each bin a set of 10 random aggregate realizations is generated. Size and backscattering cross sections are then averaged within each bin and the data are interpolated to fit the model size bins. Averaging the radar cross sections of different realizations within a given size bin is assumed to account for the variability found in populations of natural aggregates. The number of aggregates per bin

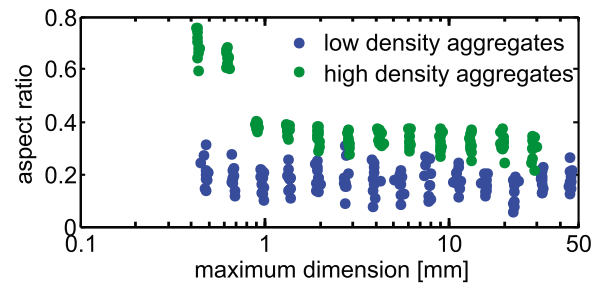


**Figure 5.** Aspect ratio (defined as the ratio between maximum vertical and maximum horizontal dimensions) for low and high density aggregate realizations. The low density aggregates are flatter, while the high density ones are thicker, almost spherical for very small sizes.

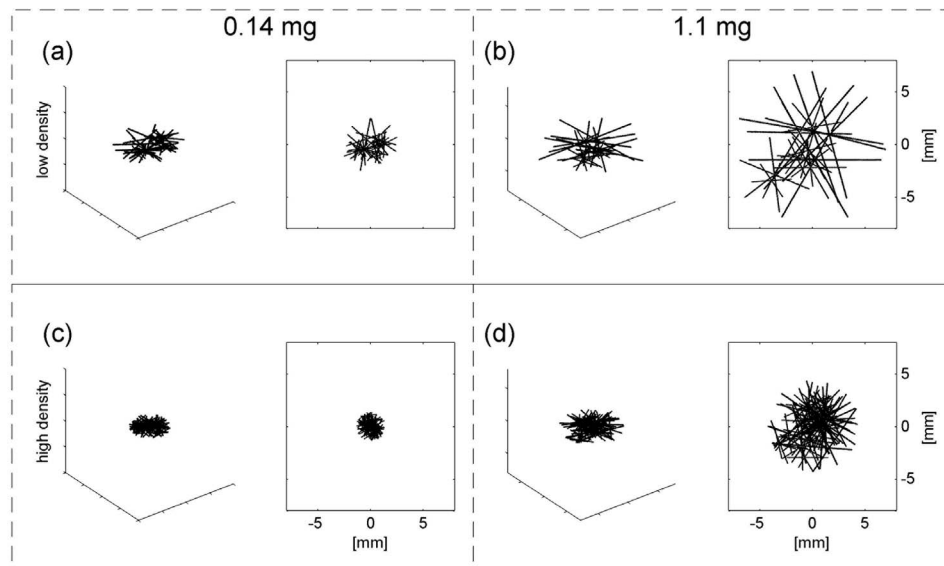


**Figure 6.** Examples of low and high density aggregate realizations. Two low density realizations for two different values of mass; (a) 0.14 and (b) 1.1 mg. (c and d) Two high density realizations for the same two respective values of mass.

was determined as the minimum number of realizations needed to obtain convergence in the backscattering cross section average value. Figure 1 (left) shows the two mass-dimensional relationships for aggregates employed in the CRM model (solid lines) with the actual mass-size for the aggregate realizations (overlapped dots). Each realization has mass and maximum dimension with a margin of error less than 5% and 3%, respectively.

### 3.2.2. Bulk Models for Aggregates

[27] GMM method results will be compared with widely used bulk models for aggregates. The bulk models represent aggregates as a spheroid or sphere with effective dielectric constants computed using the Maxwell Garnett equivalent dielectric constant formula [e.g., *Bohren and Battan*, 1980] with air being the host and ice the inclusion and the volume fraction the ratio of the ice volume to the total particle volume (i.e., of the sphere or spheroid). Four different aggregate bulk models are used in this paper and are defined as follows: an oblate spheroid model with maximum dimension and aspect ratio matching the constructed aggregate, denoted as OBS (corresponding to the FS3 model of *Botta et al.* [2010]); a second oblate spheroid model with a fixed aspect ratio of 0.6, denoted as OBS06 (note that OBS06 will be less dense compared to OBS for the same maximum dimension because OBS has a smaller aspect ratio, as shown in Figure 5); the circumscribing sphere with a diameter equal to the maximum dimension of the aggregate, denoted as SMAX; and a sphere with an equivalent radius based on the root-mean square distance of the particle mass from the center of gravity of the aggregate [*Petty and Huang*, 2010], denoted as SRMS (this sphere has a radius that is 29% larger than the one based on the radius of gyration used by *Osharin* [1994] and *Westbrook et al.* [2006]).

[28] An illustration of an aggregate realization with its representation using three of the bulk models is shown in Figure 4b (the OBS06 will have the same maximum

dimension as OBS but with a larger vertical axis). Note that three of the bulk models, OBS, OBS06 and SMAX, have the same maximum dimension as the aggregate but different shapes, and two bulk models, SMAX and SRMS, have the same shape but different maximum dimensions. Furthermore, all four bulk models have the same mass but different bulk densities leading to different dielectric constants. Also note that the aggregates constructed for the GMM model provide critical shape information for the oblate spheroid model (OBS) in terms of aspect ratio, which together with the maximum dimension and resulting density determines the effective dielectric constant. This approach constrains the value of the aspect ratio in the OBS model, which is usually a free parameter not available in the literature. The SRMS spherical model is also closely connected to the GMM aggregate model since its equivalent diameter is computed using the positions of each sphere in the cluster [*Petty and Huang*, 2010], thus it could not be defined without the GMM model. OBS06 has an aspect ratio that is chosen somewhat arbitrarily. This aspect ratio value of 0.6 appears in a paper by *Korolev and Isaac* [2003] for aggregates based on CPI data, which is not necessarily representative of the ratio of the vertical to horizontal dimensions of freely falling particles in the atmosphere. *Korolev and Isaac* [2003] note that: “The CPI imaging laser beam has an inclination  $45^\circ$  to the horizon. The natural orientation of ice particles inside the CPI sampling tube is changed due to shear and the air deceleration. The effect of shear on the orientation inside the CPI sampling tube is not clear and requires a special study.” The OBS06 results are shown to illustrate problems with arbitrary selection of shape parameters.

[29] Scattering computations for spheres and spheroids are performed using Mishchenko’s T-Matrix code [*Mishchenko et al.*, 2002] for the spheroid models (OBS and OBS06) and Mätzler’s Mie code [*Mätzler*, 2002] for the sphere models (SMAX and SRMS), the latter being a similar approach as

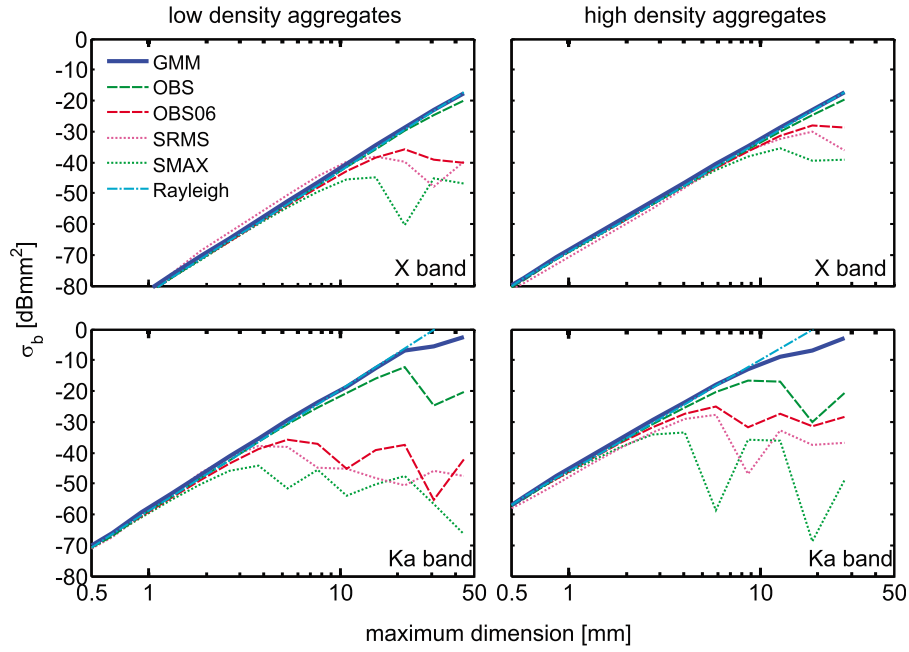


**Figure 7.** Aggregate backscattering cross sections ( $\sigma_b$ ) at vertical incidence for GMM and bulk model (OBS, OBS06, SRMS, SMAX) computations. (top) X-band (31.86 mm wavelength, i.e., 9.41 GHz) and (bottom) Ka-band (8.4 mm wavelength, i.e., 35.6 GHz). The Rayleigh scattering cross sections for a sphere are also shown. The dielectric constant used in the Rayleigh computations is the same as SMAX. (left) Low and (right) high density aggregates.

described by Haynes *et al.* [2007]. It will be shown that these models lead to different backscattering cross sections at resonance sizes for a particle of given mass. Bulk model results for aggregates will be used in conjunction with the spherical model for pristine ice to compute radar reflectivity values.

### 3.2.3. Comparisons of Backscattering Cross Sections of Aggregate Models

[30] X- and Ka-band  $\sigma_b$  at vertical incidence for aggregates are shown in Figure 7 as a function of maximum dimension. The aggregates have their maximum dimensions aligned along the horizontal plane with no canting. The GMM results (averaged in azimuth only, i.e., in the horizontal plane) are compared with the four different bulk models. Note that the  $\sigma_b$  in Figure 7 are obtained after averaging the backscattering cross sections of 10 aggregates generated at each mass/size bin shown in Figure 1. All the bulk models exhibit resonance effects for the larger sizes as evidenced by the oscillations and reduction in  $\sigma_b$ . This effect is enhanced at Ka-band and for spherical bulk models, which have lower  $\sigma_b$  values compared to the GMM results, e.g., at 5 mm sizes (small aggregates) the difference reaches 20 dB for the SMAX model. Moreover, the difference between the two spherical models at that size is close to 15 dB. The spheroidal model denoted as OBS performs much better than the other bulk models at vertical incidence, although it also starts decreasing relative to the GMM results at very large sizes. This agreement is mainly due to the fact that the OBS model replicates the vertical dimension of the aggregates much better than do the spherical models. Because the vertical dimensions of the OBS spheroids are small (Figure 5), resonance effects become observable only

at the larger sizes. The  $\sigma_b$  of the OBS06 model deviates from the GMM  $\sigma_b$  beginning at smaller sizes compared to those of OBS. Also, both spheroid models (OBS and OBS06) fail, just like the spherical models, at side incidence (i.e., viewing the particle along the horizontal plane) as shown in Figure 8. At side incidence, the maximum

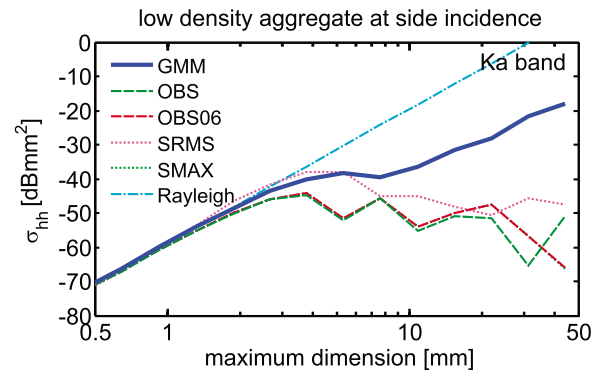


**Figure 8.** Ka-band horizontal-polarization backscattering cross sections ( $\sigma_{hh}$ ) at side incidence of aggregates for GMM and bulk model (OBS, OBS06, SRMS, SMAX) computations. Note that SMAX and OBS06 have such similar behavior and are overlapped. This plot should be compared to Figure 7 (bottom left), which shows the same set of aggregates and bulk models at vertical incidence. The Rayleigh scattering cross sections for a sphere are also shown. The dielectric constant used in the Rayleigh computations is the same as SMAX.



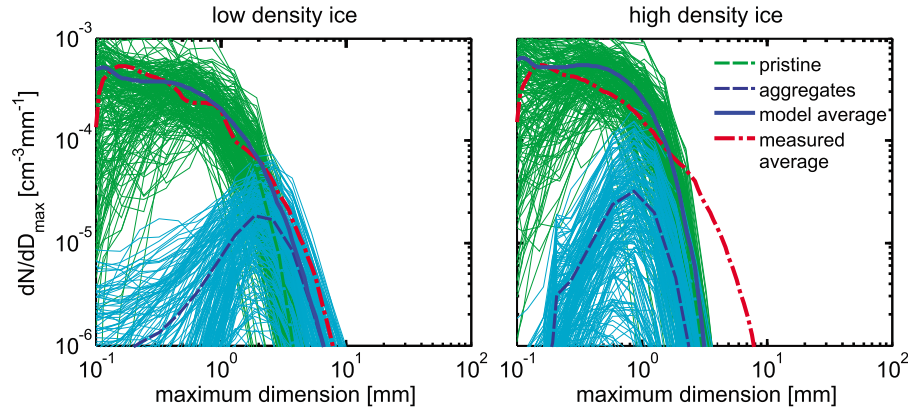


**Figure 9.** Pristine crystal and aggregates model concentration for two selected runs. The thin lines represent 200 randomly selected CRM grid-volumes extracted from the output concentration. Thick lines show averages for all CRM grid-volumes and the average concentration measured on April 8th, 2008 between 22:30 and 23:00 (red line). The two CRM runs only differ in the choice of the mass-dimensional relationships of pristine crystals and aggregates, denoted as low density and high density ice.

dimension of both spheroid models (OBS and OBS06) and the sphere (SMAX) are the same along the direction of propagation of the electromagnetic wave. Thus, in this case the OBS and OBS06 models perform just like SMAX, even though the shape, volume, bulk density and dielectric constants of the three models are different.

[31] Also shown in Figures 7 and 8 are results for Rayleigh scattering from a sphere with the same diameter and density as SMAX. It is interesting to note that for vertical incidence (Figure 7) at X-band the Rayleigh and GMM results are within 1 dB for the size range considered here (up to 30 mm and 44 mm for high and low density aggregates, respectively). At Ka-band the backscattering cross sections from the Rayleigh approximation and the GMM method are also within 1 dB for sizes up to 20 mm for low density aggregates and 9 mm for high density aggregates. The Rayleigh approximation exceeds the GMM results at Ka-band by more than 8 dB for the largest sizes. At side incidence (Figure 8) the GMM and Rayleigh results are within 1 dB up to 2.5 mm at Ka-band and their difference sharply increases beyond that, reaching 22 dB at the largest size. The vertical and side incidence results are significantly different mainly because the aggregate appears to be thicker along the direction of propagation of the electromagnetic wave at side incidence. Note that the Rayleigh results are identical at vertical and side incidence because the particle is modeled as a sphere.

#### 4. Results

[32] Figure 9 shows the pristine ice and aggregate number concentration distributions at 200 randomly selected model grid-volumes as well as the average distributions taken from all model grid-volumes between 200 m and 1000 m above ground level and after the first two hours of model “spin-up.” Also shown are the means of the model total ice size distributions and all the aircraft in situ measured particle size distributions. Figure 9 (left) shows results for a CRM simulation using the low density parameterization for ice (pristine and aggregates), while Figure 9 (right) shows

results for a different CRM simulation using the high density parameterization for ice (pristine and aggregates). The model simulation for the low density ice better resembles the observed size distributions compared to the high density simulation, although it slightly underestimates the concentration of big aggregates. The high density simulations fall significantly below the measured distributions at the larger sizes. *Avramov et al.* [2011, section 5.3] show that both simulations are in reasonable agreement with measured liquid and ice water concentration profiles. However, current in situ measurements provide no direct quantitative constraints on the CRM critical ice properties such as the maximum dimension, projected area and aspect ratio as a function of mass, which are highly variable and together strongly impact CRM simulation results. In addition, there are large uncertainties in measurements of bulk ice water content and ice particle size distributions [*Korolev et al.*, 2011]. Comparison to radar reflectivity measurements, therefore, provides a valuable independent added constraint on the actual ice particle properties.

[33] The modeled pristine crystal and aggregate size distributions are used in conjunction with the appropriate backscattering cross sections to calculate the effective radar reflectivity factor (assuming liquid water for the dielectric factor to be consistent with the radar measurements) at both X- and Ka-band for each model grid-volume. Histograms of all grid-volume radar reflectivities are compared to radar measurements. Figures 10 and 11 show results using the low-density (*Mitchell* [1996] P1d for pristine and *Kajikawa* [1989] for aggregates), and high-density (*Mitchell* [1996] P1c for pristine and *Mitchell and Heymsfield* [2005] for aggregates) mass-dimensional relationships. Also shown are comparisons of measured radar reflectivities with those calculated using the in situ size distribution measurements. The measured particle size distributions (PSDs) have been re-binned to match the size bins in the cloud model. The 2-D particle imaging probes indicate a transition from pristine crystals to aggregates between roughly 2 and 5 mm maximum dimension [*Avramov et al.*, 2011]. Therefore the measured size distributions were split into two separate

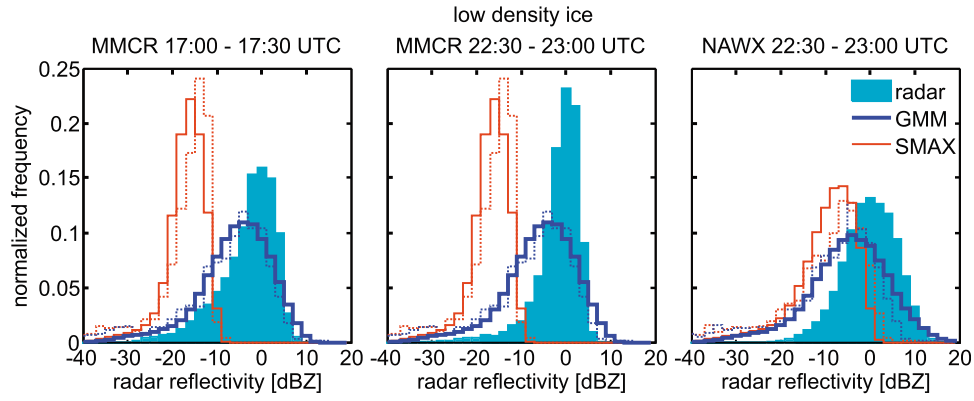


**Figure 10.** Simulated and measured radar reflectivity histograms at (left and middle) Ka and (right) X-band. The solid lines show reflectivities computed using CRM simulated PSD, while dotted lines show reflectivities computed using in situ measured PSD (same PSD data as in Figure 9). Radar measurements (MMCR and NAWX, taken on April 8th, 2008) together with GMM and the spherical bulk model SMAX simulations are shown in all panels. In this CRM model run, low density pristine crystals and aggregates are assumed.

distributions for pristine crystals and aggregates, with all particles smaller than 2 mm being pristine crystals and larger than 5 mm being aggregates, and with the concentration fraction for sizes between 2 mm and 5 mm linearly changing from zero to one.

[34] Figure 10 for low density ice shows that the differences between the GMM and spherical bulk model results can exceed 15 dB. At X-band the GMM and SMAX results are closer because the resonance effects are reduced at longer wavelengths (Figure 10, right). At Ka-band, resonance effects are enhanced, especially for the SMAX model, resulting in histograms shifted to much lower reflectivities (Figure 10, left and middle). The solid line histograms are generated based on the CRM simulated PSDs and the dotted lines are from in situ measured PSDs. Both the GMM-CRM and GMM-in situ results (solid and dotted blue lines, respectively) compare well with the measured reflectivity (shaded) histogram at both Ka- and X-band.

[35] Figure 11 shows the same histograms as in Figure 10 but for high density ice. Both the GMM-CRM and GMM-in situ results compare poorly with the radar measurements at both frequencies with histograms shifted toward much

lower reflectivities for the CRM results and much higher reflectivities for the in situ results. This result is to be expected since the measured PSDs have much higher concentration for larger particles than the CRM PSDs, leading to the higher reflectivity values. Furthermore, the increase relative to the low-density GMM-in situ calculations is the result of the greater mass, and hence  $\sigma_b$ , assigned to any hydrometeor of a given size. For a given PSD, the ice water content (IWC) scales with the mass-dimensional relationship. However, the increase in reflectivity resulting from the higher IWC associated with the measured PSDs does not compensate for the lack of the large hydrometeors (Figure 9, right) in the GMM-CRM calculations, with the net result being a shift in the histograms to lower reflectivities relative to the radar measurements. The CRM ice representations provide the critical physical link between the population PSDs, the radar reflectivity distributions and the in situ measurements. It is concluded that the low density representations of the ice hydrometeor populations provide the best overall fit between the model and the different observational data sets. Quantification of uncertainties in both measurements and simulations is

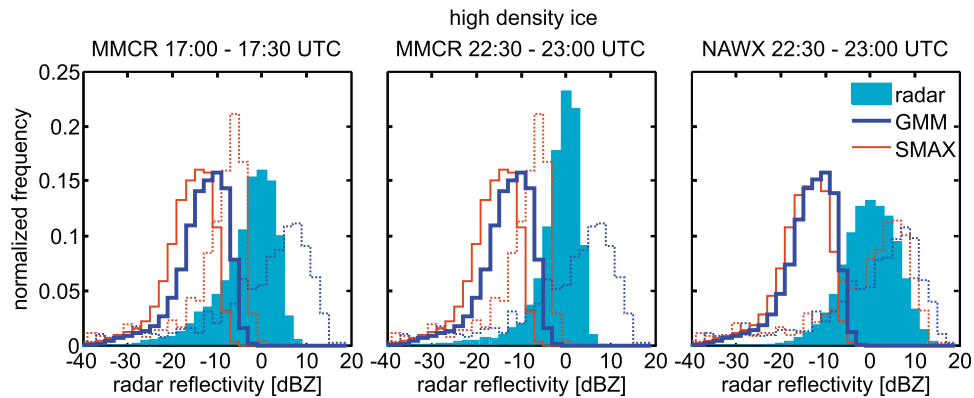


**Figure 11.** Same as Figure 10 but for high density pristine crystals and aggregates.

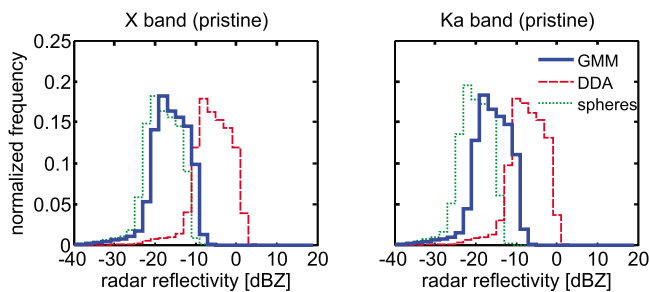


**Figure 12.** Reflectivity histograms computed using CRM simulated PSDs for the low density pristine crystals (P1d) [Mitchell, 1996] based on GMM and a spherical model, and another model (DDA) for similarly shaped crystals, but with a different mass-dimensional relationship, available from a lookup table for scattering from ice particles [Liu, 2008] (<http://cirrus.met.fsu.edu/research/scatdb.html>).

required in future work to better establish and understand the source of discrepancies.

[36] Figures 12 and 13 illustrate the importance of properly modeling all ice hydrometeors: pristine crystals and aggregates. The reflectivities are simulated using PSDs from the CRM for the two ice categories separately. The GMM and sphere results for pristine ice in Figure 12 have the same mass-dimensional relationship used for the low-density pristine crystals in the CRM. The sphere histograms have lower reflectivities compared to the GMM histograms by about 2 dB at X-band and 4 dB at Ka-band. Furthermore, the third histogram in each panel corresponds to a different (larger) mass-dimensional relationship Liu [2008] (<http://cirrus.met.fsu.edu/research/scatdb.html>). The reflectivity histograms for this case exceed the GMM histograms by about 10 dB at X-band and 8 dB at Ka-band. This effect is mostly due to the different mass-dimensional relationship. It is clear that having the proper mass-dimensional relationship for the pristine crystals is very important.

[37] Figure 13 compares the shape effects of ice aggregates on the reflectivity histograms. All five models are closer at X-band than at Ka-band because of the resonance effects being much smaller at X-band. However, even at X-band the sphere models do not generate reflectivities as high as the GMM model does. At Ka-band the differences between GMM and the sphere models (SMAX and SRMS) as well as the spheroidal model OBS06 exceed 10 dB. The closest model is the OBS, which was generated to conform to the aggregate aspect ratio, giving it an advantage over the other bulk models.

[38] These results suggest that great care should be used when evaluating models with observations, but also that much can be learned about the hydrometeor population characteristics when necessary attention is given to the details in the comparison. The reflectivity in a volume depends on the PSDs of hydrometeors, their mass, size and shape. It is necessary that all CRM assumptions about the hydrometeor populations be faithfully reproduced in the modeling of hydrometeors for radar scattering computations to obtain valid comparisons, e.g., a poor choice of mass-dimensional relationships for either the pristine crystals or aggregates in the scattering computations can have signifi-

cant impact on the reflectivity calculations (Figures 10, 11, 12 and 13). The strong dependence of the radar scattering calculations on the assumed parameters of the hydrometeor populations may be exploited to diagnose optimal values for those parameter settings in the CRM through analyses similar to that used in this study, thus strengthening the physical basis of the model ice hydrometeor representations.

## 5. Conclusions

[39] The objective of this study was to evaluate results of a CRM using cloud radar measurements. Several radar backscattering models were used to transform the CRM-produced ice hydrometeor populations to radar reflectivities at Ka- and X-band radar frequencies. It was found that a refined representation of the ice hydrometeors, both pristine crystals and their aggregates, is required in order to obtain comparable CRM-domain reflectivity histograms to actual radar measurements. An algorithm to generate realistic aggregates from a collection of pristine ice crystals, each of which is constructed from a cluster of tiny ice spheres, is an integral part of this radar scattering model. The scattering computations are performed using the Generalized Multiparticle Mie (GMM) method. These aggregates satisfy the constraints set by the component crystal type and the mass-dimensional relationship used in the CRM, but the algorithm allows their aspect ratio to adjust freely.

[40] When using the standard spherical or spheroidal (bulk model) representation for ice hydrometeors together with the CRM PSDs, reflectivity histograms were shifted below the radar measurements by more than 15 dB. Bulk model approaches were less accurate especially at Ka-band because of resonances in the backscattering cross sections for aggregate sizes exceeding half the wavelength (about 4 mm and 15 mm at Ka- and X-band, respectively), resulting in the underestimation of radar reflectivity. The spheroidal model OBS produced better results than the spherical models, because the aspect ratios of the spheroids were specified to conform to the shape of the generated aggregates. However, the spheroidal model OBS06, which had a fixed aspect ratio of 0.6 produced similar results as the spherical models. Finally, the radar calculations were particularly sensitive to the mass-dimensional relationships used for both pristine ice crystals and aggregates, warranting a caution about the use of

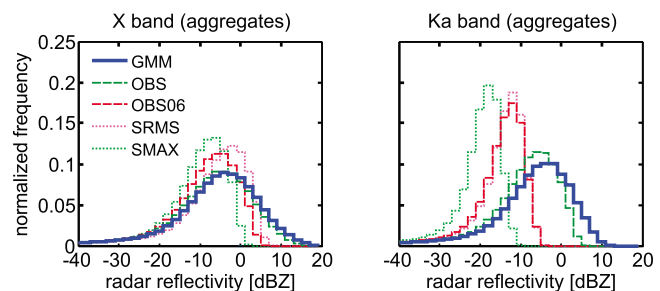


**Figure 13.** Reflectivity histograms computed using CRM simulated PSDs for the low density ice crystal aggregate model [Kajikawa, 1989]. GMM results are compared with those corresponding to the oblate spheroidal (OBS and OBS06) and spherical (SMAX and SRMS) bulk models.

backscattering cross section results from databases if the mass-dimensional relationships differ from the desired ones.

[41] It is anticipated that at frequencies above Ka-band, e.g., W-band (94 GHz, 3.19 mm wavelength), bulk models of aggregates and pristine crystals will experience resonance effects at all sizes of aggregates greater than about 1.6 mm. With the proliferation of cloud-research radars operating at these millimeter wave band frequencies it is essential to consider refined models such as the one described here. Multiple frequency measurements (W-, Ka- and X-band) from the same volume will provide very strong tests of the fidelity of the model hydrometeor populations as the different frequencies will accentuate contributions from different parts of the PSD.

[42] Comparison of CRM products with in situ measurements alone is not sufficiently definitive in discriminating between the model parameterizations. It is demonstrated here that the addition of radar-model comparison analysis leads to more discrimination, if refined scattering models of ice particles are incorporated in the evaluations. As the community moves toward more sophisticated CRM microphysics representations, such as the one described by *Avramov et al.* [2011], multiple observational sources including reflectivity and Doppler velocity measurements at several radar frequencies will be of great value for model evaluations.

[43] **Acknowledgments.** The work was supported by the Office of Biological and Environmental Research of the U.S. Department of Energy grant DE-FG02-05ER64058 as part of the Atmospheric System Research Program. This research used resources of the National Energy Research Scientific Computing Center, which is supported by the Office of Science of the U.S. Department of Energy under contract DE-AC02-05CH11231. A.A., A.S.A. and A.M.F. were supported by the DOE Office of Science, Office of Biological and Environmental Research, through Interagency Agreements DE-AI02-06ER64173 and DE-AI02-08ER64547, and the NASA Radiation Sciences Program.

## References

- Ackerman, A. S., O. B. Toon, and P. V. Hobbs (1995), A model for particle microphysics, turbulent mixing, and radiative-transfer in the stratocumulus-topped marine boundary layer and comparisons with measurements, *J. Atmos. Sci.*, **52**(8), 1204–1236, doi:10.1175/1520-0469(1995)052<1204:AMFPMT>2.0.CO;2.
- Avramov, A., and J. Y. Harrington (2010), The influence of parameterized ice habit on simulated mixed-phase arctic clouds, *J. Geophys. Res.*, **115**, D03205, doi:10.1029/2009JD012108.
- Avramov, A., et al. (2011), Towards ice formation closure in Arctic Mixed-phase boundary layer clouds during ISDAC, *J. Geophys. Res.*, doi:10.1029/2011JD015910, in press.
- Aydin, K., and T. A. Seliga (1984), Radar polarimetric backscattering properties of conical graupel, *J. Atmos. Sci.*, **41**, 1887–1892, doi:10.1175/1520-0469(1984)041<1887:RPBPOC>2.0.CO;2.
- Aydin, K., and T. M. Walsh (1999), Millimeter wave scattering from spatial and planar bullet rosettes, *IEEE Trans. Geosci. Remote Sens.*, **37**(2), 1138–1150, doi:10.1109/36.752232.
- Aydin, K., T. A. Seliga, and V. N. Bringi (1984), Differential radar scattering properties of model hail and mixed phase hydrometeors, *Radio Sci.*, **19**, 58–66, doi:10.1029/RS019i001p00058.
- Battán, L. J., and B. M. Herman (1962), The radar cross sections of “spongy” ice spheres, *J. Geophys. Res.*, **67**, 5139–5145, doi:10.1029/JZ067i013p05139.
- Böhm, H. (1989), A general equation for the terminal fall speed of solid hydrometeors, *J. Atmos. Sci.*, **46**(15), 2419–2427, doi:10.1175/1520-0469(1989)046<2419:AGEFTT>2.0.CO;2.
- Böhm, J. P. (1992a), A general hydrodynamic theory for mixed-phase microphysics. Part I: Drag and fall speed of hydrometeors, *Atmos. Res.*, **27**(4), 253–274, doi:10.1016/0169-8095(92)90035-9.
- Böhm, J. P. (1992b), A general hydrodynamic theory for mixed-phase microphysics. Part II: Collision kernels for coalescence, *Atmos. Res.*, **27**(4), 275–290, doi:10.1016/0169-8095(92)90036-A.
- Böhm, J. P. (1992c), A general hydrodynamic theory for mixed-phase microphysics. Part III: Riming and aggregation, *Atmos. Res.*, **28**(2), 103–123, doi:10.1016/0169-8095(92)90023-4.
- Böhm, J. P. (1994), Theoretical collision efficiencies for riming and aerosol impaction, *Atmos. Res.*, **32**(1–4), 171–187, doi:10.1016/0169-8095(94)90058-2.
- Böhm, J. P. (1999), Revision and clarification of “A general hydrodynamic theory for mixed-phase microphysics,” *Atmos. Res.*, **52**(3), 167–176, doi:10.1016/S0169-8095(99)00033-2.
- Böhm, J. P. (2004), Reply to comment on “Revision and clarification of ‘A general hydrodynamic theory for mixed-phase microphysics’ [Böhm J.P., 1999, *Atmos. Res.* **52** (3), 167–176],” *Atmos. Res.*, **69**(3–4), 289–293, doi:10.1016/j.atmosres.2003.10.001.
- Bohren, C. F., and L. J. Battán (1980), Radar backscattering by inhomogeneous precipitation particles, *J. Atmos. Sci.*, **37**, 1821–1827, doi:10.1175/1520-0469(1980)037<1821:RBBIPP>2.0.CO;2.
- Botta, G., K. Aydin, and J. Verlinde (2010), Modeling of microwave scattering from cloud ice crystal aggregates and melting aggregates: A new approach, *IEEE Geosci. Remote Sens. Lett.*, **7**(3), 572–576, doi:10.1109/LGRS.2010.2041633.
- de Boer, G., T. Hashino, and G. J. Tripoli (2010), Ice nucleation through immersion freezing in mixed-phase stratiform clouds: Theory and numerical simulations, *Atmos. Res.*, **96**, 315–324, doi:10.1016/j.atmosres.2009.09.012.
- Fridlind, A. M., A. S. Ackerman, G. McFarquhar, G. Zhang, M. R. Poellot, P. J. DeMott, A. J. Prenni, and A. J. Heymsfield (2007), Ice properties of single-layer stratocumulus during the Mixed-Phase Arctic Cloud Experiment (M-PACE): 2. Model results, *J. Geophys. Res.*, **112**, D24202, doi:10.1029/2007JD008646.
- Goldstein, H., C. Pool, and J. Safko (2001), *Classical Mechanics*, 3rd ed., Addison Wesley, Boston, Mass.
- Grecu, M., and W. S. Olson (2008), Precipitating snow retrievals from combined airborne cloud radar and millimeter-wave radiometer observations, *J. Appl. Meteorol. Climatol.*, **47**, 1634–1650, doi:10.1175/2007JAMC1728.1.
- Haynes, J. M., R. T. Marchand, Z. Luo, A. Bodas-Salcedo, and G. L. Stephens (2007), A multi-purpose radar simulation package: QuickBeam, *Bull. Am. Meteorol. Soc.*, **88**, 1723–1727, doi:10.1175/BAMS-88-11-1723.
- Intergovernmental Panel on Climate Change (IPCC) (2007), *Climate Change 2007: The Physical Science Basis. Contribution of Working Group I to the Fourth Assessment Report of the Intergovernmental Panel on Climate Change*, edited by S. Solomon et al., Cambridge Univ. Press, Cambridge, U. K.
- Ishimoto, H. (2008), Radar backscattering computations for fractal-shaped snowflakes, *J. Meteorol. Soc. Jpn.*, **86**, 459–469, doi:10.2151/jmsj.86.459.
- Kajikawa, M. (1989), Observation of the falling motion of early snowflakes. Part II: On the variation of falling velocity, *J. Meteorol. Soc. Jpn.*, **67**(5), 731–738.
- Klein, S. A., et al. (2009), Intercomparison of model simulations of mixed-phase clouds observed during the ARM Mixed-Phase Arctic Cloud Experiment. Part I: Single layer cloud, *Q. J. R. Meteorol. Soc.*, **135**, 979–1002, doi:10.1002/qj.416.
- Kollias, P., E. E. Clothiaux, M. A. Miller, E. P. Luke, K. L. Johnson, K. P. Moran, K. B. Widener, and B. A. Albrecht (2007), The Atmospheric Radiation Measurement Program cloud profiling radars: Second-generation sampling strategies, processing, and cloud data products, *J. Atmos. Oceanic Technol.*, **24**, 1199–1214, doi:10.1175/JTECH2033.1.
- Korolev, A. V., and G. Isaac (2003), Roundness and aspect ratio of particles in ice clouds, *J. Atmos. Sci.*, **60**, 1795–1808, doi:10.1175/1520-0469(2003)060<1795:RAAROP>2.0.CO;2.
- Korolev, A. V., E. F. Emery, J. W. Strapp, S. G. Cober, G. A. Isaac, M. Wasey, and D. Marcotte (2011), Small ice particles in tropospheric clouds: Fact or artifact? Airborne Icing Instrumentation Evaluation Experiment, *Bull. Am. Meteorol. Soc.*, doi:10.1175/2010BAMS3141.1, in press.
- Liu, G. (2008), A database of microwave single-scattering properties for nonspherical ice particles, *Bull. Am. Meteorol. Soc.*, **89**(10), 1563–1570, doi:10.1175/2008BAMS2486.1.
- Longtin, D. R., C. F. Bohren, and L. J. Battán (1987), Radar backscattering by large, spongy ice oblate spheroids, *J. Atmos. Oceanic Technol.*, **4**, 355–358, doi:10.1175/1520-0426(1987)004<0355:RBLISI>2.0.CO;2.
- Marshall, J. S., and K. L. S. Gunn (1952), Measurement of snow parameters by radar, *J. Meteorol.*, **9**, 322–327, doi:10.1175/1520-0469(1952)009<0322:MOSPBR>2.0.CO;2.
- Matrosov, S. Y. (2007), Modeling backscatter properties of snowfall at millimeter wavelengths, *J. Atmos. Sci.*, **64**, 1727–1736, doi:10.1175/JAS3904.1.

- Mätzler, C. (2002), MATLAB functions for Mie scattering and absorption, version 2, *IAP Res. Rep. 02-11*, 26 pp., Inst. für angewandte Phys., Univ. Bern, Bern.
- McFarquhar, G. M., et al. (2011), Indirect and Semi-Direct Aerosol Campaign (ISDAC): The impact of arctic aerosols on clouds, *Bull. Am. Meteorol. Soc.*, 92, 183–201, doi:10.1175/2010BAMS2935.1.
- Meneghini, R., and L. Liao (1996), Comparisons of cross sections for melting hydrometeors as derived from dielectric mixing formulas and a numerical method, *J. Appl. Meteorol.*, 35, 1658–1670, doi:10.1175/1520-0450(1996)035<1658:COCSFM>2.0.CO;2.
- Mishchenko, M. I., L. D. Travis, and A. A. Lacis (2002), *Scattering, Absorption, and Emission of Light by Small Particles*, 3rd rev. electron. ed., Cambridge Univ. Press, Cambridge, U. K.
- Mitchell, D. L. (1996), Use of mass- and area-dimensional power laws for determining precipitation particle terminal velocities, *J. Atmos. Sci.*, 53, 1710–1723, doi:10.1175/1520-0469(1996)053<1710:UOMAAD>2.0.CO;2.
- Mitchell, D. L., and A. J. Heymsfield (2005), Refinements in the treatment of ice particle terminal velocities, highlighting aggregates, *J. Atmos. Sci.*, 62, 1637–1644, doi:10.1175/JAS3413.1.
- Mitchell, D. L., R. Zhang, and R. L. Pitter (1990), Mass-dimensional relationships for ice particles and the influence of riming on snowfall rates, *J. Appl. Meteorol.*, 29(2), 153–163, doi:10.1175/1520-0450(1990)029<0153:MDRFIP>2.0.CO;2.
- Moran, K. P., B. E. Martner, M. J. Post, R. A. Kropfli, D. C. Welsh, and K. B. Widener (1998), An unattended cloud-profiling radar for use in climate research, *Bull. Am. Meteorol. Soc.*, 79, 443–455, doi:10.1175/1520-0477(1998)079<0443:AUCPRF>2.0.CO;2.
- Morrison, H., et al. (2009), Intercomparison of model simulations of mixed-phase clouds observed during the ARM Mixed-Phase Arctic Cloud Experiment, Part II: Multi-layered cloud, *Q. J. R. Meteorol. Soc.*, 135, 1003–1019, doi:10.1002/qj.415.
- O'Brien, S. G., and G. H. Goedecke (1988), Scattering of millimeter waves by snow crystals and equivalent homogeneous symmetric particles, *Appl. Opt.*, 27(12), 2439–2444, doi:10.1364/AO.27.002439.
- Osharin, A. (1994), Scattering of millimeter radio waves by dry snowflakes, paper presented at Geoscience and Remote Sensing Symposium, IEEE, New York.
- Petty, G. W., and W. Huang (2010), Microwave backscatter and extinction by soft ice spheres and complex snow aggregates, *J. Atmos. Sci.*, 67, 769–787, doi:10.1175/2009JAS3146.1.
- Protat, A., D. Bouniol, E. J. O'Connor, H. K. Baltink, J. Verlinde, and K. Widener (2011), CloudSat as a global radar calibrator, *J. Atmos. Oceanic Technol.*, 28, 445–452, doi:10.1175/2010JTECHA1443.1.
- Pruppacher, H. R., and J. D. Klett (1997), *Microphysics of Clouds and Precipitation*, Kluwer Acad., Norwell, Mass.
- Stevens, D. E., A. S. Ackerman, and C. S. Bretherton (2002), Effects of domain size and numerical resolution on the simulation of shallow cumulus convection, *J. Atmos. Sci.*, 59(23), 3285–3301, doi:10.1175/1520-0469(2002)059<3285:EODSAN>2.0.CO;2.
- Tang, C., and K. Aydin (1995), Scattering from ice crystals at 94 and 220 GHz millimeter wave frequencies, *IEEE Trans. Geosci. Remote Sens.*, 33(1), 93–99, doi:10.1109/36.368218.
- Toon, O. B., C. P. McKay, T. P. Ackerman, and K. Santhanam (1989), Rapid calculation of radiative heating rates and photodissociation rates in inhomogeneous multiple scattering atmospheres, *J. Geophys. Res.*, 94(D13), 16,287–16,301, doi:10.1029/JD094iD13p16287.
- Westbrook, C. D., R. C. Ball, and P. R. Field (2006), Radar scattering by aggregate snowflakes, *Q. J. R. Meteorol. Soc.*, 132, 897–914, doi:10.1256/qj.05.82. [Corrigendum, *Q. J. R. Meteorol. Soc.*, 134, 547–548, doi:10.1002/qj.233, 2008.]
- Wolde, M., and A. Pazmany (2005), NRC dual-frequency airborne radar for atmospheric research, paper presented at 32nd International Conference on Radar Meteorology, Am. Meteorol. Soc., Albuquerque, N. M.
- Xu, Y.-L. (1995), Electromagnetic scattering by an aggregate of spheres, *Appl. Opt.*, 34(21), 4573–4588, doi:10.1364/AO.34.004573.
- Xu, Y.-L., and B. Å. S. Gustafson (2001), A generalized multiparticle Mie-solution: Further experimental verification, *J. Quant. Spectrosc. Radiat. Transf.*, 70(4–6), 395–419, doi:10.1016/S0022-4073(01)00019-X.
- A. S. Ackerman and A. M. Fridlind, NASA Goddard Institute for Space Studies, 2880 Broadway, New York, NY 10025, USA.
- A. E. Avramov, Department of Earth, Atmospheric, and Planetary Sciences, 77 Massachusetts Ave., Rm. 54-1415, Massachusetts Institute of Technology, Cambridge, MA 02139-4307, USA.
- K. Aydin and G. Botta, Department of Electrical Engineering, Pennsylvania State University, 301 Electrical Engineering East, University Park, PA 16802, USA. (gub13@psu.edu)
- G. M. McFarquhar, Department of Atmospheric Sciences, University of Illinois at Urbana-Champaign, 105 S. Gregory St., Urbana, IL 61801-3070, USA.
- M. Wolde, Flight Research Laboratory, Institute for Aerospace Research, National Research Council, Ottawa, U-61, 1200 Montreal Rd., Ottawa, ON K1A 0R6, Canada.
- J. Verlinde, Department of Meteorology, Pennsylvania State University, 503 Walker Bldg., University Park, PA 16802, USA.